aerospace

MDPI

Article

Experimental and Correction Methods for Responsivity Temperature Dependence in the SWIR Bands of a Spaceborne Scanning Polarimeter

Hao Dong [1,2], Zhenhai Liu [1], Xuefeng Lei [1,2], Congfei Li [1], Fei Tao [1,*], Xinxin Zhao [1,2], Mingchun Ling [1], Lei Yan [1], Zhen Sun [1], Qiang Cong [3], Peng Zou [1], Maoxin Song [1] and Jin Hong [1]

[1] Anhui Institute of Optics and Fine Mechanics, Hefei Institutes of Physical Science, Chinese Academy of Sciences, Hefei 230031, China
[2] University of Science and Technology of China, Hefei 230026, China
[3] DFH Satellite Co., Ltd., Beijing 100094, China
* Correspondence: taofei@aiofm.ac.cn

Abstract: Photodetector spectral responsivity is usually affected by photosensitive surface temperatures. The Photosensitive Surface Temperatures (PSTs) of the long wavelength-type InGaAs detector used in the Polarized Scanning Atmospheric Corrector (PSAC), which adopts an active Constant-Current Cooling (CCC) scheme, can be changed with ambient temperature. To correct this responsivity temperature characteristic, a Responsivity Temperature Dependence Correction (RTDC) model was established with parameters obtained using an instrument-level experiment. Moreover, a detector-level experiment under ambient conditions was also explored to acquire model parameters. The instrument-level and detector-level experimental results show that the responsivity of a PSAC 2250 nm channel operating on orbit (PST ≈ -65 °C) with a 35 °C PST difference is reduced by approximately 1.2% and 1.5% compared with a laboratory-based radiometric test (PST ≈ -30 °C). The 1.08% responsivity change (-61 °C $<$ PST < -38 °C) in the temperature drift simulation experiment is reduced to approximately 0.38% and 0.34%, respectively. The consistency between the two experimental results preliminarily verifies the substitutability of this detector-level experiment for this type of detector. The RTDC experiments are applicable to other spaceborne remote sensors. The detector-level experiment explored herein provides a reference for realizing RTDC under ambient temperature conditions at low costs.

Keywords: HJ-2; PSAC; atmosphere correction; polarization; experimental methods; temperature dependence

check for updates

Citation: Dong, H.; Liu, Z.; Lei, X.; Li, C.; Tao, F.; Zhao, X.; Ling, M.; Yan, L.; Sun, Z.; Cong, Q.; et al. Experimental and Correction Methods for Responsivity Temperature Dependence in the SWIR Bands of a Spaceborne Scanning Polarimeter. *Aerospace* **2023**, *10*, 200. https://doi.org/10.3390/aerospace10020200

Academic Editor: Pierre Rochus

Received: 29 November 2022
Revised: 7 February 2023
Accepted: 18 February 2023
Published: 20 February 2023

1. Introduction

The Polarized Scanning Atmospheric Corrector (PSAC) is a wide-swath spaceborne scanning polarimeter with high polarization accuracy that is used to detect atmospheric aerosol parameters, provide atmospheric correction parameters for other remote sensors on the same satellite platform, and improve the quantification of other sensors [1–5]. For aerosol retrieval over land, the required spectral and spatial distribution information changes dramatically with the surface reflectance and terrain. The PSAC is equipped with three Shortwave Infrared (SWIR) channels (1380 nm, 1610 nm, and 2250 nm) to accurately obtain surface radiation information through land–atmosphere decoupling, thus providing key information for overland aerosol retrieval [6]. The radiation characteristics of these long-wavelength-type InGaAs detectors used in the 2250 nm channel are greatly affected by the Photosensitive Surface Temperatures (PSTs) [7]. With the active Constant-Current Cooling (CCC) scheme adopted in PSAC SWIR detectors, the PST drift is expected to be approximately ± 3 °C in each orbit [8]. Furthermore, the working temperature differences in PSAC detectors between on-orbit operations and the laboratory-based radiometric test limit the on-orbit absolute radiometric accuracy. Therefore, Responsivity Temperature Dependence Correction (RTDC) must be performed; otherwise, the retrieval results obtained for the atmospheric parameters are directly affected [9,10].

For some remote sensors working in harsh environments, responsivity temperature characteristic measurement and RTDC are important steps in the calibration process. Researchers have performed extensive research on this topic. Jack et al. [11] focused on the problem wherein Moderate Resolution Imaging Spectroradiometer (MODIS) detectors may change with the temperature of the Focal Plane Assembly (FPA) affected by MODIS and the environment without precise temperature control of FPA. An instrument-level thermal vacuum experiment was conducted before the launch of the MODIS by simulating three different ambient temperatures and using an integrating sphere light source to obtain the RTDC coefficients of the solar reflection channels, and correction was applied to the onboard data pre-processing. Barnes et al. [12] performed similar work to obtain the RTDC coefficient of the Sea-viewing Wide Field-of-View Sensor (SeaWiFS) before launch, and the NASA Ocean Biology Processing Group (OBPG) calibration and validation team computed a revised set of RTDC for SeaWiFS with on-orbit periodic lunar calibration data and removed the significant periodic departures in the Near Infrared (NIR) bands (765 nm and 865 nm) from the mission-long trends [13]. As a preferred verification benchmark for atmospheric aerosol satellite remote sensing, the Aerosol Robotic Network (AERONET) suffers from similar problems wherein the responsivity of the 1020 nm channel in its core instrument CE-318 needs to be corrected for the temperature effect of its detector and the filter [14,15]. Research has shown that the temperature drift of the operating environment may result in an Atmospheric Optical Depth (AOD) inversion error up to 0.02 [16]. To obtain the RTDC coefficient for each CE-318, Holben [12,17] measured this coefficient based on a temperature chamber in the laboratory, Berjón et al. [14] and Andor et al. [15] compared the synchronous observation results of various instruments and reference instruments in the field, and Chen et al. [18] acquired a coefficient with the improved Langley method. To determine the RTDC of the Directional Polarimetric Camera (DPC), P. Yao et al. [19] constructed the relationship between the radiation response and the detector assembly temperature based on a thermal control design and a thermal vacuum experiment; the responsivity temperature dependence coefficient was obtained after dark signal correction and frame transfer correction.

In the above research, a common strategy used to study the RTDC of remote sensors is instrument-level experiments. This method can obtain relatively accurate and reliable coefficients that benefit from the integrity of the experimental instrument. However, a challenging problem that arises in this method is high experimental costs and rigorous experimental conditions. We therefore analyzed a detector-level experiment and investigated whether its experimental results are substitutable for this type of detector.

In this study, we first established an RTDC model of the PSAC. Then, the model coefficients over a large temperature range were obtained through instrument-level experiments in a thermal vacuum condition and ambient laboratory temperature. Moreover, based on targeted control of the identified experimental interference factors, the model coefficients were also determined through detector-level experiments at an ambient laboratory temperature. Finally, the models obtained from two types of tests and the corresponding temperature drift correction results were compared to verify the validity and substitutability of the detector-level experiment. The detector-level experiment explored in this article for obtaining the RTDC coefficients under ambient laboratory temperature conditions has benefits in terms of its low cost and easy implementation. This article provides a reference for determining the responsivity temperature dependence characteristics of other spaceborne remote sensors through ground detector temperature experiments on similar detectors.

2. Instrument, Model, and Method

2.1. Instrument

The Chinese environmental protection and disaster monitoring satellite constellation Huanjing Jianzai-2 (HJ-2) A/B satellites were launched on 27 September 2020. HJ-2A and HJ-2B, with the same configuration, run in a sun-synchronous orbit, and the local time of descending node is about 10:30 a.m. They are arranged in a 180° phase to obtain a higher time resolution [3]. Each satellite carries a 16 m Charge-Coupled Device (CCD) camera, a Hyperspectral Imager (HSI), an Infrared Spectroradiometer (IRS), and the PSAC. The PSAC provides the other remote sensors with the atmospheric parameters required for atmospheric correction to further improve the application efficiency of remote sensors and the level of remote sensing quantification. The main structure of the PSAC is shown in Figure 1 [3].

The measurement principle of the PSAC is the same as that of the American Aerosol Polarimetry Sensor/Glory Mission (APS/Glory) [20]. It adopts a simultaneous polarization measurement scheme based on a combination of split-aperture and split-amplitude components and acquires 9 bands and 4 polarization analyzers' relative azimuths (for a total of 36 channels) to obtain spectral intensity information simultaneously in the field-of-view range of $-32.5^\circ \sim +32.5^\circ$ for cross-track scanning. The schematic diagram of the optical path of the PSAC is shown in Figure 2. The PSAC adopts two dual detectors per band to measure I_0, I_{45}, I_{90}, and I_{135}. These four linearly polarized units with different polarizations analyze relative azimuths. Additionally, the main specifications of the PSAC are shown in Table 1.

In principle, the PSAC can determine the first three Stokes parameters in the Equation (1) of the target linear polarization state [2]:

$$S = \begin{bmatrix} I \\ Q \\ U \\ V \end{bmatrix} = \begin{bmatrix} I_0 + I_{90} \\ I_0 - I_{90} \\ I_{45} + I_{135} \\ V \end{bmatrix} = \begin{bmatrix} I_{45} + I_{135} \\ I_0 - I_{90} \\ I_{45} + I_{135} \\ V \end{bmatrix} \tag{1}$$

where S represents the Stokes vector; $[I,Q,U,V]$ are the four Stokes parameters of a plane wave; I is the light intensity information, which is the sum of the responses of two channels with polarization azimuths that differ by 90°; Q is the linear polarization in the horizontal direction; U is the linearly polarized component at an angle of 45° from the horizontal direction; and V is the circularly polarized component, which is much smaller than the other three components in natural scenes and is often ignored [21].

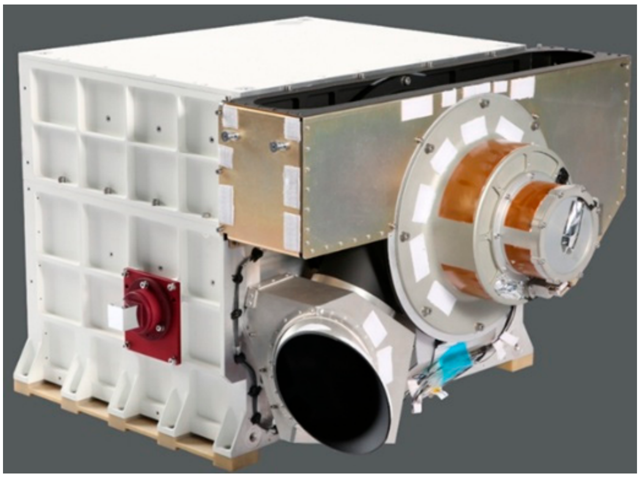

Figure 1. Main structure of the PSAC [3].

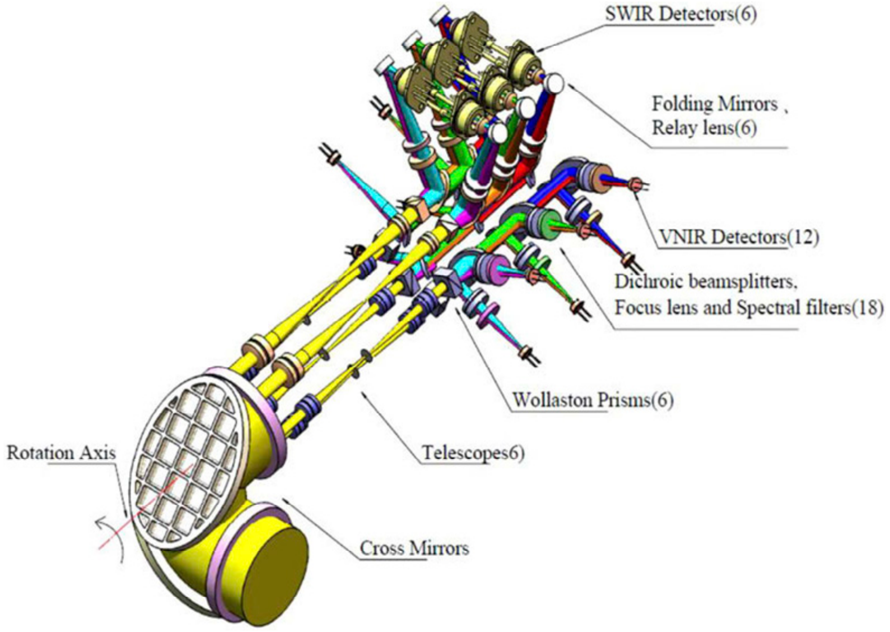

Figure 2. Schematic diagram of the optical path of the PSAC. It adopts a simultaneous polarization measurement scheme based on a combination of split-aperture and split-amplitude components and acquires 9 bands and 4 polarization analyzers' relative azimuths (for a total of 36 channels) to obtain spectral intensity information simultaneously in the field-of-view range of −32.5°~ + 32.5° for cross-track scanning.

Table 1. Main specifications of the PSAC.

Parameter	Unit	Value
Swath	km	≥800
Instantaneous Field of View (IFOV)	°	0.52
Resolution at nadir	km	≤6@645
Wavelength bands	nm	410, 443, 555, 670, 865,910, 1380, 1610, 2250
Polarization analyzers' relative azimuths	°	0, 45, 90, 135
Radiometric accuracy	%	≤5
Polarimetric accuracy	/	≤0.005 ($p < 0.3$)

As detailed in Table 1, the PSAC is equipped with 2250 nm polarization channels for the observation and acquisition of intensity and polarization information of the underlying surface for better land–atmosphere decoupling of other channels [6]. Previous studies on PSAC have shown that the temperatures of the heat sink and the photosensitive surface of the detectors in 2250 nm channels need to be kept below −20 °C and −50 °C, respectively, to better suppress noise and background radiation [7,8]. A schematic diagram of the SWIR detector assembly structure is shown in Figure 3. Two SWIR detectors in the same band are mounted back to back on the heat sink, and the cold shield is installed in front of the detectors. The only SWIR detector assembly consisting of these components is connected to the radiator plate through the heat pipe. The SWIR detector components adopt an active–passive temperature control scheme—that is, an active CCC scheme based on Thermo-Electric Coolers (TECs) built into each detector and a passive cooling scheme based on a radiator plate connected to the external heat sink of the SWIR detectors, which can reduce the PST fluctuation with high control accuracy, low power consumption, and low computing resource requirements. However, this active CCC and passive radiative cooling scheme cannot hold the PST stable, and it will vary with the temperature of the external conditions. Actually, the temperature drift of the cry radiator in one orbit is expected to be generally less than ±3 °C, and thus the PST will fluctuate synchronously in this small range. Moreover, the temperature difference between the photosensitive surface of the detector and the heat sink will be very limited; it can be achieved only by the active cooling of the TECs inside the detector. Therefore, it will be difficult to obtain the low PST required for the on-orbit (PST ≈−65 °C) operation under higher ambient temperatures, such as PSAC laboratory-based radiometric test conditions. The temperature comparison of detector assembly during two operation conditions is presented in Table 2. There is a PST difference of approximately 35 °C when PSAC is in on-orbit operation (PST ≈ −65 °C) compared with its laboratory-based radiometric test (PST ≈ −30 °C).

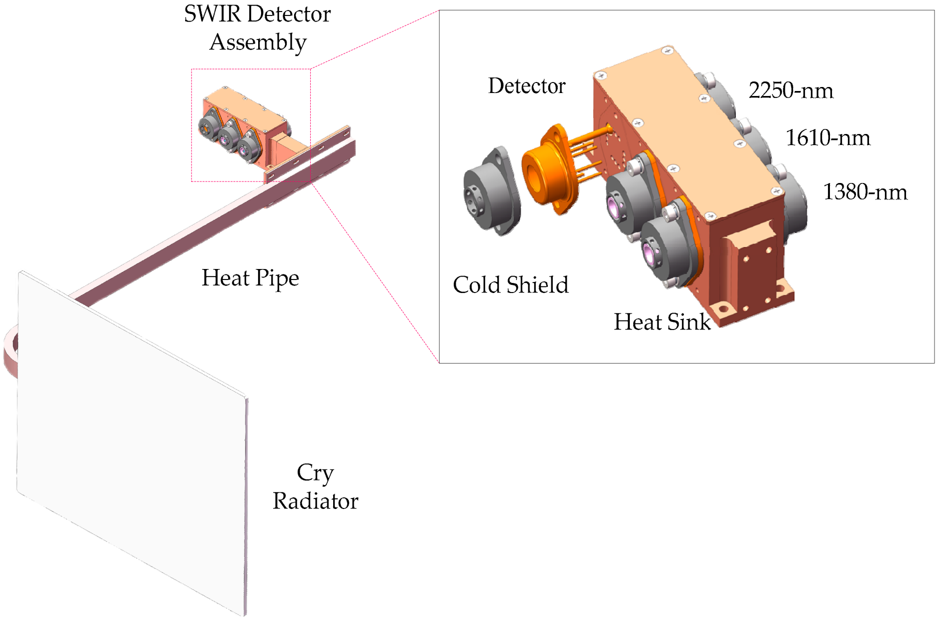

Figure 3. The SWIR detector assembly. Two SWIR detectors in the same band are mounted back to back on a heat sink. The SWIR detectors and cold shield are mounted on the heat sink and connected to the cry radiator through the heat pipe.

Table 2. PSAC SWIR detector assembly temperature comparison under two operating environments.

	Laboratory-Based Radiometric Test	**On-Orbit Operation**
Main structure temperature	≈20 °C	≈20 °C
Heat sink temperature	≈20 °C	≈−15 °C
PST	≈−30 °C	≈−65 °C

Generally, the photoelectric characteristics of the detector are always affected by the PST. The spectral photosensitivity of the detector of 2250 nm channels at two temperatures provided by the manufacturer is shown in Figure 4. The PST difference between the on-orbit operation (PST ≈ −65 °C) and laboratory-based radiometric test (PST ≈ −30 °C) is expected to reduce its responsivity by more than 1%. As seen in Table 1, the PSAC radiometric accuracy specification is better than 5%. In addition, as the manufacturer of the PSAC, referring to MODIS which is the typical remote sensor for land–atmosphere radiation detection [22], we expect the radiation accuracy of the PSAC to reach 3.5%. To ensure the detection accuracy of atmospheric parameters, it is necessary to perform PSAC RTDC.

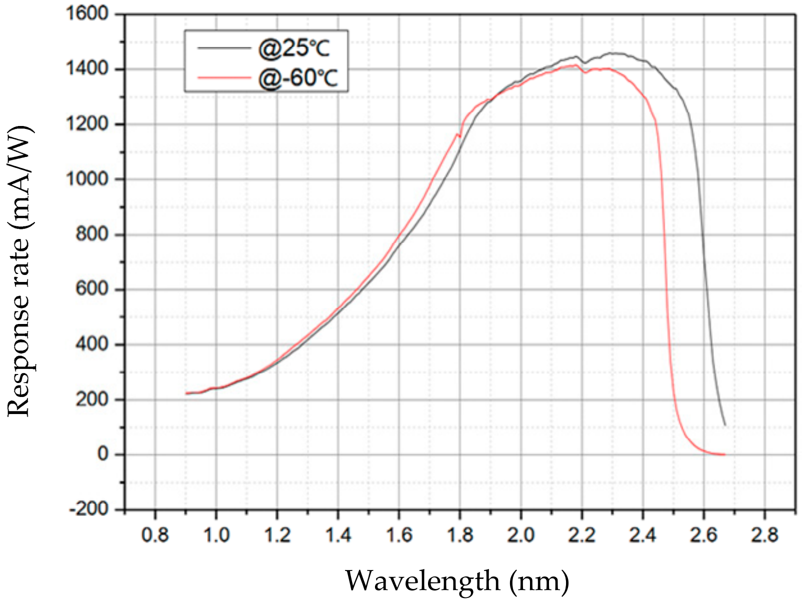

Figure 4. Example of the photosensitivity temperature dependence of detector used in the PSAC 2250 nm channel. Two PSTs used for comparison are independent of RTDC experiments.

2.2. RTDC Model

The PSAC operation temperature differences between on-orbit and laboratory environments were compared to analyze the responsivity temperature dependence sources of the PSAC. With the instrument thermal controller, a sub-system of a spacecraft maintaining a stable spacecraft temperature in the harsh space environment, the temperatures of the PSAC structure and the optical assemblies were consistent in the two conditions. However, with the active–passive cooling scheme, the heat sink and the photosensitive surface faced a temperature difference of nearly 35 °C. The PSAC is equipped with a DC Restore (DCR) circuit [23], which adopts a direct current recovery loop circuit to realize the dynamic correction of signal drift of a front-end circuit output, a signal amplification and conditioning circuit, and a photoelectric detector. With the cooperation of the DCR function and dark reference, background radiation response in different heat sink temperatures is subtracted in each scan. We determined that the PST difference is the main source of PSAC responsivity change. Thus, research focusing on the responsivity temperature dependence of the detectors used in the PSAC 2250 nm channel was performed in this study. As for the detectors used in 1380 nm and 1610 nm channels, their temperature dependence is very small and can be ignored.

The formula for performing RTDC is shown in Equation (2). G(T) is the RTDC model for the 2250 nm channel. T represents the PST. DN(T) and DN(T_{ref}) are the Digital Number (DN) values of the PSAC when the PSTs are T and T_{ref}, respectively. T_{ref} represents the reference temperature. With G(T), PSAC response in different PSTs is corrected to that in T_{ref}.

$$DN(T_{ref}) = DN(T)/G(T) \tag{2}$$

In the measurement and calculation of G(T), DN(T_{ref}) is used as a reference to normalize the DN values at other PSTs in the same radiation, and G(T) is obtained using cubic spline fitting normalization results. T_{ref} is set to −30 °C, which is the same as that in the laboratory-based radiometric test, and T is varied in the range of $-65\ ^{\circ}C < T < -30\ ^{\circ}C$ at least to ensure the applicability of G(T) in on-orbit and ground environments.

2.3. Experimental Method

To obtain the coefficient of RTDC model G(T) over a large temperature range, the basic principle of this experiment is to obtain the normalized results of radiation response by changing the PST of the detector under the same radiation conditions. The model

$G_{det}(T)$ and $G_{ins}(T)$ were obtained by detector-level experiments and instrument-level experiments, respectively. To meet the range of T, two different experimental conditions were set in experiments. The experimental structure of detector-level and instrument-level experiments is shown in Figure 5.

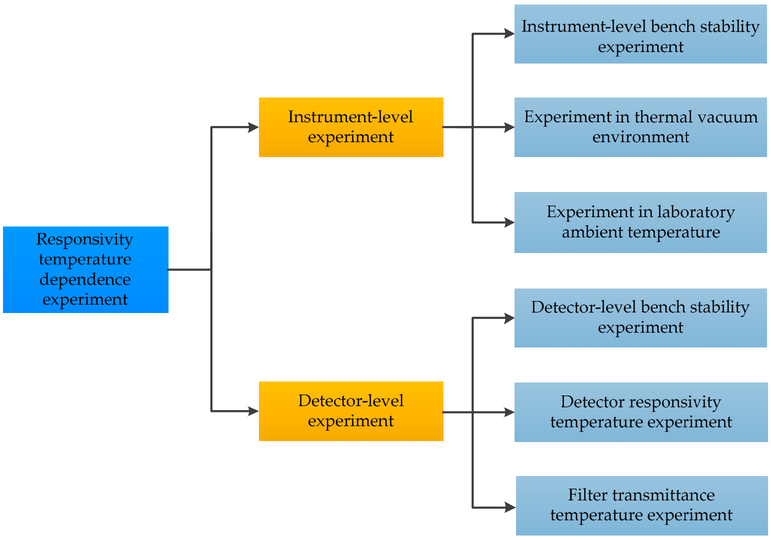

Figure 5. Diagram of the RTDC experimental structure.

The instrument-level experiment contains three sub-experiments. First, a bench stability experiment was conducted. Then, combined with PSAC active–passive detector temperature control, the experiment was conducted in a vacuum chamber that can simulate the on-orbit operation environment (T < −35 °C) and ambient laboratory temperature (T > −35 °C). A schematic diagram of the instrument-level RTDC experimental method is shown in Figure 6. By adjusting the CCC current, the PST could span the PSAC operation conditions on orbit and in the laboratory (−65 °C < T < −25 °C). With a constant radiation source provided by the integrating sphere, $G_{ins}(T)$ was obtained by fitting the relationship between the PST and the PSAC DN normalization results with a cubic spline function.

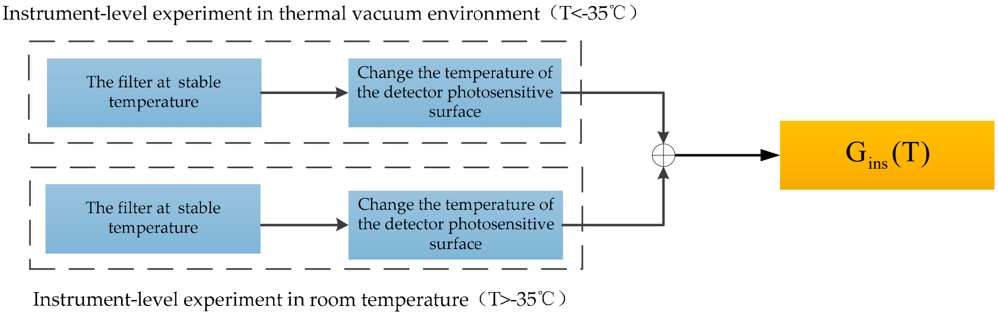

Figure 6. Schematic diagram of the instrument-level RTDC experimental method.

However, the accuracy of $G_{ins}(T)$ over two instrument-level sub-experiments faced challenges of inconsistent experimental conditions, such as different optical path transmittance and different background radiation associated with a changing heat sink temperature. The difference in background radiation was mitigated with the DCR function using the PSAC fixed-point observation mode with a dark reference provided by a chopper. As for different optical path transmittance, normalization based on overlapping temperatures between two sub-experiments was applied. The corresponding formula is shown in

Equation (3), where $g_{vac}(T)$ and $g_{lab}(T)$ represent the DN values in the thermal vacuum sub-experiment and the ambient laboratory temperature sub-experiment, respectively.

$$G_{ins}(T) = \frac{g_{vac}(-35)}{g_{vac}(-30)} \cdot \frac{g_{lab}(T)}{g_{lab}(-35)} \ (T > -35°C) \tag{3}$$

The detector-level experiment contains three sub-experiments; a schematic diagram of the detector-level RTDC experimental method is shown in Figure 7. $G_{fil}(t)$ represents the filter transmissivity temperature model, where t represents the temperature of the filter. Limited to the temperature difference between the photosensitive surface and heat sink of the detector being attained only by the active cooling of the TEC inside the detector, the detector-level experiment was divided into two sub-experiments with different heat sink cooling conditions, one under a water-cooling condition ($T < -50$ °C) and one under ambient laboratory temperature ($T > -50$ °C), to meet the range of T. Furthermore, a filter transmittance temperature experiment was conducted considering the temperature characteristics of the filter.

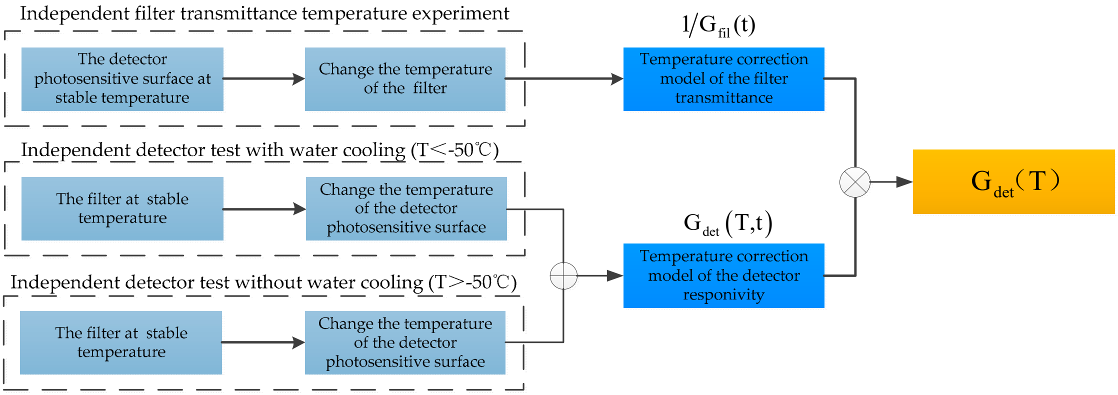

Figure 7. Schematic diagram of the detector-level RTDC experimental method.

Compared with the instrument-level experiment, to meet the substitution and accuracy of $G_{det}(T)$, the detector-level experiment not only needs to solve the internal interferences caused by its own characteristics, such as the changing background radiation and detector dark current, but also needs to overcome the external interferences from the inconsistent operation state compared with the instrument-level experiment. Based on the dark reference provided by the chopper, the internal interferences at different temperatures had little influence on $G_{fil}(t)$ measurement. As for the most important external interference factor, the filter transmissivity temperature characteristic is corrected by $G_{fil}(t)$.

In the detector-level experiment, the filter was mounted on the cooling shield due to the space limits. With the temperature effect of narrow-channel filters, their transmittance may change with the water-cooling temperature [24,25]. In the filter transmittance experiment, T was fixed while t varied with the circulating water cooler setting temperature. The detector response current of the filter temperature at 20 °C was used as a benchmark to normalize the response currents at other filter temperatures. $G_{fil}(t)$ was obtained by cubic fitting of this normalization result. With this, the formula for obtaining $G_{det}(T)$ after $G_{fil}(t)$ correction is shown in Equation (4), where $G_{det}(T, t)$ represents the detector response normalization results under different T and t.

$$G_{det}(T) = G_{det}(T, t)/G_{fil}(t) \tag{4}$$

3. Experimental Setup

3.1. Instrument-Level Experiment

A diagram of the instrument-level sub-experiment in the thermal vacuum condition is shown in Figure 8. The on-orbit operation environment of the PSAC was established in the vacuum chamber by the CS-1800 space environment simulation system. The PSAC was installed on the base plate of the vacuum chamber, and the fixed-point observation mode was used with a chopper to substitutability observe the integrating sphere and the dark reference. With the PSAC thermal control system, the temperature of the heat sink was maintained at approximately −15 °C, and the temperature of the optical components was approximately 20 °C. The PST was set to $-75\ ^\circ\mathrm{C} < T < -35\ ^\circ\mathrm{C}$ with the temperature controller of the detector. The stability of the integrating sphere radiance was greater than 2‰/h, and its radiance was monitored synchronously during the experiment.

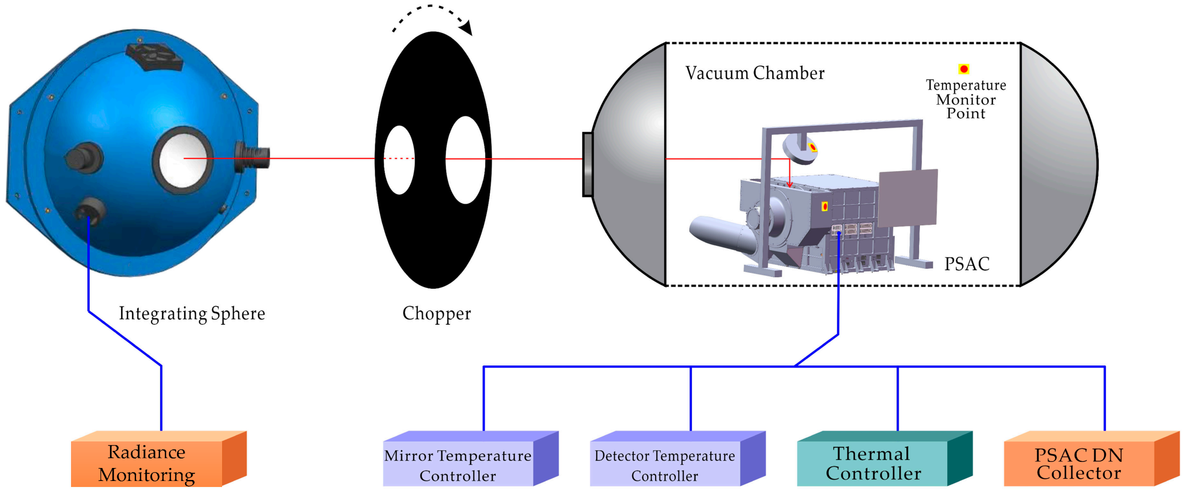

Figure 8. Schematic diagram of the instrument-level thermal vacuum sub-experiment. The PSAC was installed on the base plate of the vacuum chamber, and the fixed-point observation mode was used with a chopper to substitutability observe the integrating sphere and the dark reference. A turning light path was installed to ensure that the light source was incident to the PSAC. Temperature monitoring was performed for the PSAC body, the planar mirror, the vacuum chamber, and other key positions.

To reduce the influence of background radiation and dark current on $G_{ins}(T)$ measurement, based on the signal acquisition of the PSAC adopting an Alternating Current (AC) coupling design, a chopper was used to modulate the light source and ensure normal data acquisition. The shape of the chopper was a symmetrical open-hole disc, and the disc was sprayed with an extinction black lacquer. The stepper motor drove the disc to rotate at a uniform speed, and the rotation speed matched the PSAC sampling time sequence. When the PSAC observed a dark reference, the DCR function was implemented to establish a zero-radiation reference.

Limited by the PSAC installation state in the chamber, a turning light path was installed to ensure that the light source was incident to the PSAC, and a heating plate was mounted on the back of the planar mirror to reduce the distortion of the mirror, which would otherwise result in light path offsets at large temperature differences. In the experiment, the reflectance of the mirror and the vacuum chamber port window remained basically unchanged. Although their polarization could have caused a change in the polarization component, I in Equation (1) was relatively stable and had little influence on the $G_{ins}(T)$ measurement. To monitor the operation state of the PSAC in the experiments, temperature sensors were added to the PSAC body, the planar mirror, the vacuum chamber, and other key positions. Based on this thermal vacuum experimental condition, $G_{ins}(T)$ ($T < -50\ ^\circ\mathrm{C}$) was measured, and an instrument-level bench stability experiment was also conducted.

In the instrument-level sub-experiment in the ambient laboratory temperature, the PSAC also observed the integrating sphere through a chopper. With the operation of the active–passive detector temperature controller, the temperature of the heat sink was close to the ambient temperature, which limited the PST to higher than −35 °C.

3.2. Detector-Level Experiment

A schematic diagram of the detector-level experiment is shown in Figure 9. The detectors and cold shield were installed on the heat sink covered with an electromagnetic shielding box, and the integrating sphere was observed through the filter and chopper. A Keithley 2614B digital source meter with a measurement accuracy of 100 fA was used to measure the detector response current. The PST of the detector was controlled with a Hamamatsu C1103-05 closed-loop detector temperature controller; its stability was better than 0.1 °C. The heat sink was installed on the heat exchanger, which connected to the DX-4015 circulating water cooler through a circulating water pipe. The temperature of the key components, such as the filter and the heat sink, was measured to monitor the operational states of the equipment during the experiment. Based on this experimental condition, $G_{det}(T)$ was measured, and a detector-level bench stability experiment was conducted first.

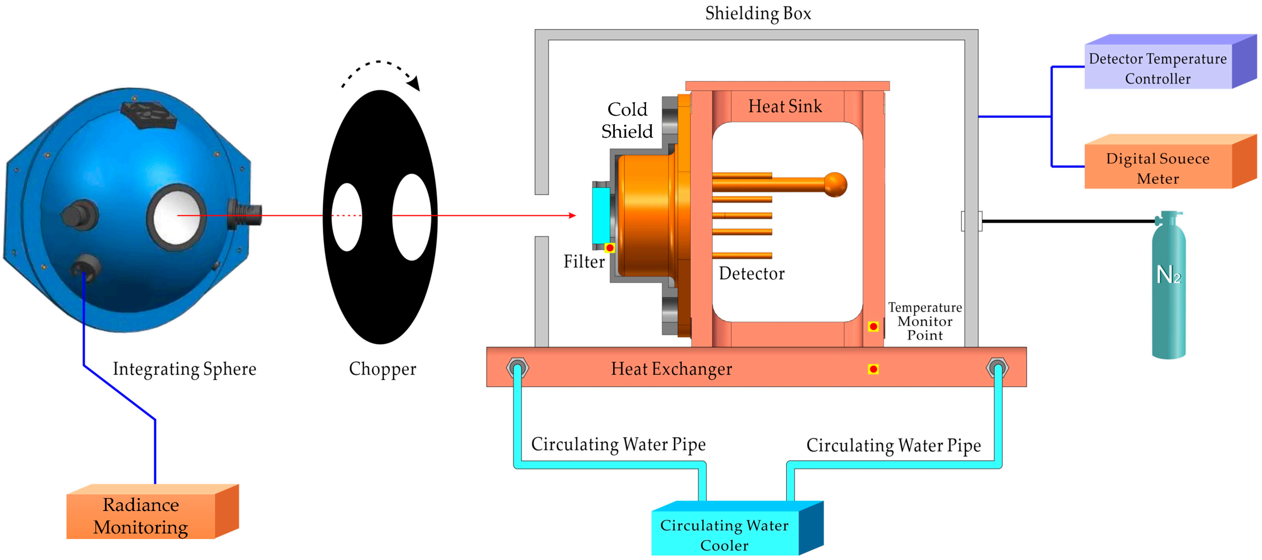

Figure 9. Schematic diagram of the detector-level experiment. The SWIR detector assembly was installed on the heat exchanger, which connected to the circulating water cooler through the circulating water pipe. The integrating sphere was observed through the filter and the window of the shielding box with the chopper.

To ensure the accuracy of the $G_{det}(T)$, the identified internal and external interference factors in the detector-level experiments were controlled separately. For the internal interference factors such as dark current and background radiation, based on their temperature-related characteristics, a cooling shield was installed in front of the detector window, and a water cooler was connected to the heat exchanger to reduce the background radiation of each component. The dark current was suppressed by reducing PST with C1103-05. With the near-real-time dark reference provided by the chopper, the internal interference factors were removed further.

Furthermore, the detector-level experiment faced external interference factors caused by differences in the instrument-level experiments. The factors and corresponding solutions can be divided into the following categories:

1. The lack of optical–mechanical components results in differences in the spectral response range and the field of view, as well as resulting in more serious stray light interference. In the detector-level experiment, the filter of the same batch used in the PSAC was installed before the cooling shield to ensure a consistent spectral response range. Because of the temperature characteristics of these narrow-channel filters, a transmittance temperature correction experiment was conducted. The field of view of the detector was limited by the cooperation of the cooling shield window and

electromagnetic shielding box opening. To suppress stray light, a matte flannelette was installed on the interior of the shielding box.

2. The absence of electromagnetic shielding and signal processing components makes it easier to couple the common frequency interference and the noise associated with experimental equipment. For this, a shielding box was tightly connected to the heat exchanger. The detector response current was measured by a digital source table through shielded twisted pairs, and the terminal was wrapped with aluminum foil to reduce electromagnetic coupling. The integration time of the digital source table was set to 50 ms to further reduce the presence of random noise.
3. In the detector-level experiment, the room temperature fluctuations affect the temperature stability of the equipment. Additionally, the heat sink temperature is lower than the ambient laboratory temperature; this may lead to a transmissivity decrease in the optical components due to condensation. To address these issues, an insulating sponge was pasted to the outside of the circulating water pipe to reduce the impact of ambient laboratory temperature fluctuation. Multi-layer Insulation (MLI) foils and a matte flannelette were adhered to the thermistor surface to reduce the temperature differences from the target. Nitrogen was continuously injected into the shielding box at a constant low speed during the experiment to prevent condensation in the detector window and filter. A rubber dehumidifier was used, which can avoid temperature changes after moisture absorption.

4. Results and Discussion

4.1. Instrument-Level Experiment Results

4.1.1. Instrument-Level Bench Stability Experiment Results

This instrument-level bench stability experiment in a thermal vacuum environment was performed to verify the temperature control effect and radiation response stability of the PSAC. The results of the bench stability experiment are shown in Figure 10. The PSAC continuously observed the integrating sphere for approximately 9 min, and 544 sets of data were collected. Based on the dark reference provided by the chopper and the PSAC DCR function, the DN fluctuated by approximately 0.75%. The temperatures of the heat sink, photosensitive surface, and main light path components were stable. The results show that in the instrument-level thermal vacuum environment, the turning optical path and temperature control effect were relatively stable, thus providing a basis for $G_{ins}(T)$ measurement.

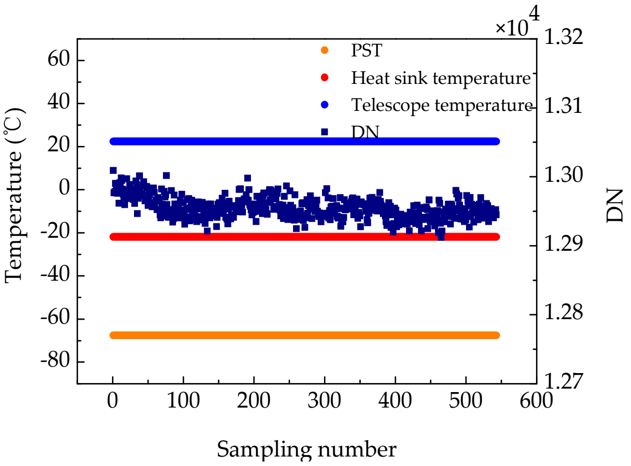

Figure 10. Results of the instrument-level stability experiment. The DN fluctuated by approximately 0.75%, and the temperatures of the heat sink, photosensitive surface, and the turning optical path were stable.

4.1.2. Instrument-Level Responsivity Temperature Dependence Experiment Results

The instrument-level experiment was divided into two sub-experiments with different operating environments to ensure the temperature range of the photosensitive surface. The $G_{ins}(T)$ results are shown in Figure 11, which shows that the responsivity of the 2250 nm channel was positively correlated with the temperature of the photosensitive surface. This instrument-level experiment determined that the responsivity was reduced by approximately 1.3% when the PSAC operated on orbit ($T \approx -30$ °C) compared with the laboratory-based radiometric test ($T \approx -65$ °C), with around 35 °C PST difference. Therefore, it is necessary to implement RTDC for the PSAC; otherwise, a large error will be introduced in the retrieval results of aerosol parameters. In Figure 11, we can see that the PST distribution was irregular and was affected by the ambient temperature under the active–passive temperature control scheme.

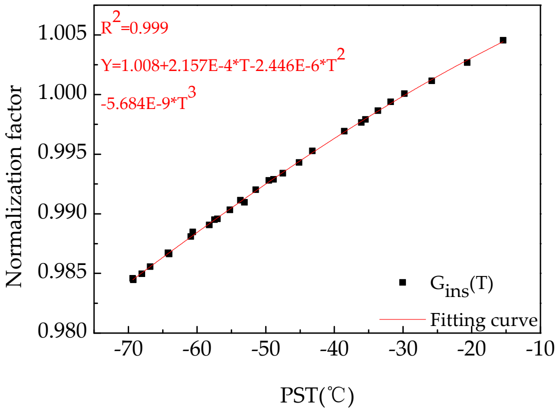

Figure 11. Results of $G_{ins}(T)$. This instrument-level experiment determined that the responsivity was reduced by approximately 1.3% when the PSAC operated on orbit compared to the laboratory-based radiometric test, with around 35 °C PST difference.

The error sources of instrument-level experiments were analyzed to determine their impact on the measurement of $G_{ins}(T)$ and the PSAC RTDC results. The random errors include the instability of light source radiance, stray light in the laboratory, instability of the PST, and nonlinearity and instability of the PSAC 2250 nm channel's radiation response. The stability of the integrating sphere radiance was greater than 2‰/h. The influence of stray laboratory light was limited to when the field of view of the PSAC was 0.52°. The combined standard uncertainty of nonlinear and unstable radiation response of the PSAC 2250 nm channel was better than 1.17% in the laboratory-based radiation test, and it was smaller when the PST was at an on-orbit operation temperature. Moreover, a systematic error may be caused by the chopper, which cannot provide an ideal dark reference with the stray light in the laboratory. The influence of this error is also limited because the response of the PSAC to the chopper is less than 1% of that of the light source. With multiple measurements and normalizing fitting, the influence of these errors on $G_{ins}(T)$ measurement is further limited, ensuring the accuracy of the instrument-level experiments.

4.2. Detector-Level Experiment Results

4.2.1. Detector-Level Bench Stability Experiment Results

A detector-level bench stability experiment was performed first to verify the temperature control effect for key components and the stability of the detector radiation response. In this sub-experiment, the circulating water-cooling temperature was set to -15 °C, the temperature controller of the detector was set to -65 °C to suppress the interference of dark current and background radiation response as much as possible, the integral time of the digital source table was set to 50 ms, and the light source was continuously observed for approximately 7 min. After dark count deduction and averaging, 55 effective response currents of the detector were obtained according to the rotation sequence of the chopper. The experimental results are shown in Figure 12. The response current fluctuation was approximately 0.19%, and the temperature fluctuations of the filter, heat sink, and heat exchanger were less than 0.02 °C. The stability results suggest that the design of the detector-level experiment was reasonable, the temperature of each component was stable, and the electromagnetic interference in the experimental environment was effectively shielded. Thus, this bench provided a good experimental basis for conducting independent filter transmittance temperature experiments and independent detector responsivity temperature dependence experiments.

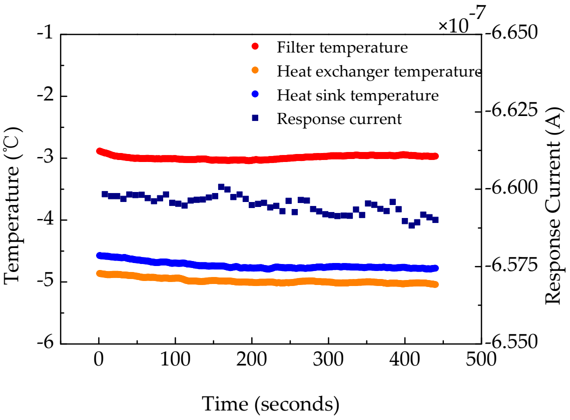

Figure 12. Results of the detector-level bench stability experiment. The response current fluctuation was approximately 0.19% during the experiment, and the temperature fluctuations of the filter, heat sink, and heat exchanger were less than 0.02 °C.

4.2.2. Filter Transmittance Temperature Experiment Results

Based on the detector-level experiment bench, the filter transmissivity test was carried out to correct the influence of filter temperature characteristics in $G_{det}(T)$ measurement. In this experiment, the PST was fixed to −65 °C by the temperature controller to mitigate dark current and noise issues as much as possible. The set temperature of the circulating water cooling (T_{cwc}) was varied in the range of −25 °C< T_{cwc} < 20 °C at a step size of 5 °C, thus indirectly controlling the filter and heat sink temperature. $F_{fil}(t)$ was obtained by conducting cubic spline fitting on the normalized results after light source radiance correction. The $F_{fil}(t)$ is shown in Figure 13; the transmittance change in the filter is inversely proportional to its temperature, and the result indicates that the filter transmittance changes by approximately 1.20% as t decreases from 20 °C to −15 °C. The temperature differences between the filter and circulating water cooler setting in experiments were influenced by the ambient laboratory temperature.

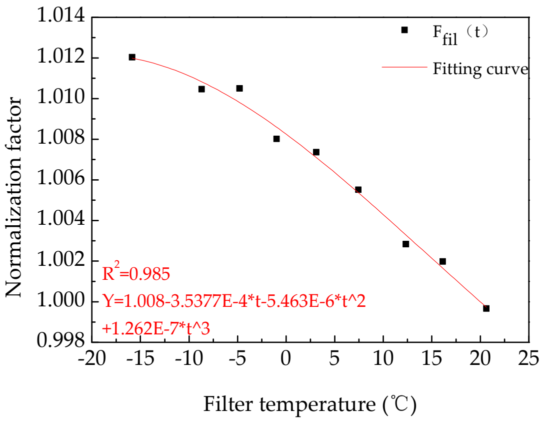

Figure 13. Experimental results of $F_{fil}(t)$. The transmittance change exhibited by the filter was approximately 1.20% as t decreased from 20 °C to −15 °C.

4.2.3. Independent Detector Responsivity Temperature Dependence Experiment Results

In the sub-experiment with four heat sink cooling temperatures, detector response currents for the same light source were measured as the PST varied. The current results before and after filter transmittance temperature correction are shown in Figure 14. The experimental results show that the response currents of the detectors were positively related to the PST, and the relative change trend remained basically constant at different heat sink temperatures. This meant that the variations in the PST of the detector were the main cause of the changes in the responsivity that occurred at the same heat sink temperature. The four response current curves after filter transmittance correction were nearly coincident, which not only verified the validity of the filter transmittance correction process but also confirmed the effectiveness of the approximate real-time dark background provided by the chopper. By averaging the correction results at the same PST, the response currents produced under the heat sink cooling sub-experiment with a filter temperature of 20 °C were obtained.

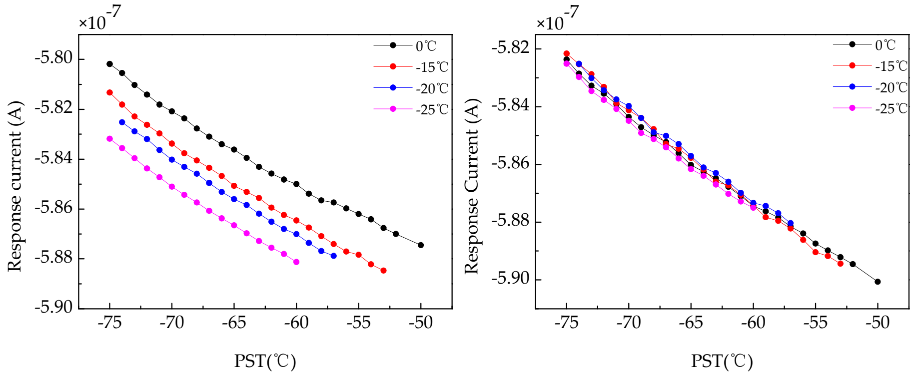

(**a**) (**b**)

Figure 14. Detector response current temperature curves at four heat sink temperatures: (**a**) before $F_{fil}(t)$ correction; (**b**) after $F_{fil}(t)$ correction.

Combined with the instrument-level sub-experiment without water cooling, the $G_{ins}(T)$ was obtained by cubic spline fitting the response current normalization results with the PST of the detector, and the results are shown in Figure 15. Similar to the instrument-level experiment results, the responsivity change trend is inversely proportional to the PST. This detector-level experiment determined that the responsivity was reduced by approximately 1.5% when the PSAC operated on orbit ($T \approx -65$ °C) compared with the laboratory-based radiometric test ($T \approx -30$ °C), with around 35 °C PST difference.

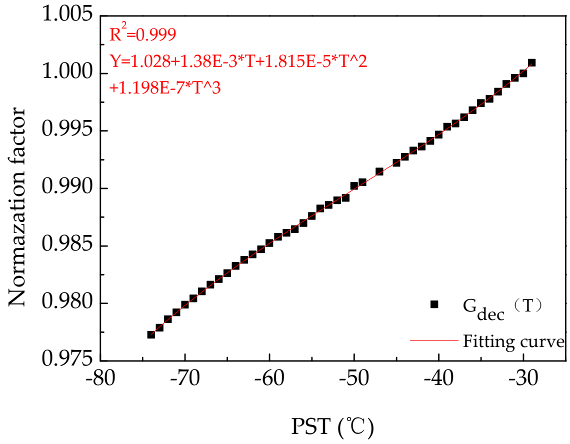

Figure 15. Experimental results of $G_{det}(T)$. This detector-level experiment determined that the responsivity was reduced by approximately 1.5% when the PSAC operated on orbit ($T \approx -65$ °C) compared with the laboratory-based radiometric test ($T \approx -30$ °C), with around 35 °C PST difference.

The error sources of detector-level experiments were analyzed to determine their impact on the measurement of $G_{det}(T)$ and $F_{fil}(t)$. The random errors include the instability of light source radiance, stray light in the laboratory, common frequency interference and noise, temperature instability of detector photosensitive surface and filter, and nonlinearity and instability of detector radiation response. The stability of the integrating sphere radiance was greater than 2‰/h. The results of the detector-level bench stability experiment have shown that temperature fluctuation and common frequency interference are effectively suppressed. The response linearity of the detector is about 100% according to the report provided by the manufacturer. Similar to the instrument-level test, the chopper may cause system error in the detector-level test, and its influence is also limited. With multiple measurements and normalizing fitting, the influence of these errors on $G_{det}(T)$ and $F_{fil}(t)$ measurement is further limited, ensuring the accuracy of the detector-level experiment.

To further verify the effectiveness of the condition control measures and dark count subtraction methods used in the detector-level experiment with large temperature ranges of the heat sink, the normalized results of the responsivity temperature dependence curves measured in two detector-level sub-experiments with different heat sink cooling conditions were compared. The comparison of the responsivity temperature dependence results is shown in Figure 16. The difference between the two sets of results was less than 0.05% after performing temperature correction on the filter transmittance. These results suggest that the condition control measures adopted in the detector-level experiment were effective and reduced the influences of various factors on the experimental results. In particular, based on the dark reference provided by the chopper dark reference, the background radiation response at different heat sink temperatures was reduced. Thus, the accuracy of the experimental results was improved and provided a good basis for obtaining responsivity temperature dependence results, ensuring the substitutability of the detector-level experiment.

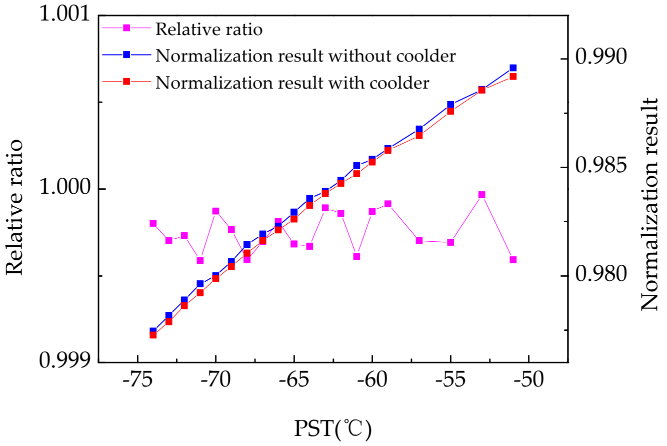

Figure 16. G(T) consistency comparison across different heat sink temperatures. The difference between the two sets of results was less than 0.05% after performing temperature correction on the filter transmittance.

4.3. Comparison of the Responsivity Temperature Dependence Results and the RTDC Effect

A comparison between the G(T) values obtained in the instrument-level and detector-level experiments was applied to verify the substitution of the detector-level experiment in RTDC. The comparison is shown in Figure 17. According to two experimental results, the responsivity of the 2250 nm channel in the on-orbit PSAC ($T \approx -65$ °C) decreased by 1.3% and 1.5%, compared with those yielded based on a laboratory-based radiometric test ($T \approx -30$ °C). As seen in Figure 17, at $T < -30$ °C, the two sets of experimental results displayed similar trends that were consistent with the temperature change. The effectiveness of detector-level experiments was basically verified, but there were still some differences. $G_{det}(T)$ shows nonlinear change with T, and the relative change in responsivity is greater compared with $G_{ins}(T)$.

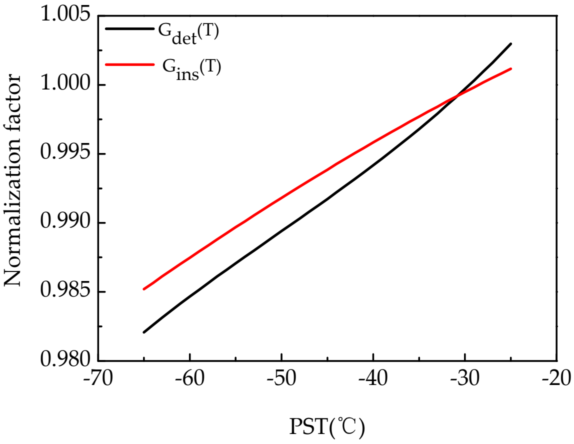

Figure 17. Comparison between the detector-level and instrument-level experimental results. $G_{det}(T)$ shows nonlinear change with PST, and the relative change in responsivity is greater compared with $G_{ins}(T)$. This difference may be that the detectors used in the two experiments were not from the same batch of products. Using $G_{det}(T)$ to correct changes in PSAC responsivity within a large temperature range may cause deviation.

The reason for this difference may be that the detectors used in the two experiments were not acquired from the same batch of products; notably, unlike the customized detectors used in the PSAC, off-the-shelf products were used in the detector-level experiment. Additionally, due to the different doping concentrations used by certain technologies in production, the responsivity temperature dependence may have varied [26]. Using $G_{det}(T)$ to correct changes in PSAC responsivity on a large temperature range may cause deviation. Therefore, in the detector-level experiment, detectors from the same batch as that used in the remote sensor needed to be selected to avoid the impact of batch differences on the experimental results.

In instrument-level and detector-level experiments, G(T) was obtained with only one detector measurement dataset. The responsivity temperature dependences of two detectors of the same batch used in PSAC, divided into four photosensitive surfaces based on the instrument-level experimental results, were compared to verify the universality of $G_{ins}(T)$. The comparison results are shown in Figure 18; they indicate that the responsivity temperature dependences of the four elements were generally consistent, and the maximum relative deviation was 0.11% in the range of -25 °C < T < -70 °C. Therefore, the $G_{ins}(T)$ obtained with this instrument-level experiment could be used to correct the responsivity temperature dependence of other detectors of the same batch.

To further compare the G(T) temperature dependence correction results of the two experiments, in the instrument-level thermal vacuum experiment, the PST was controlled in the range of -61 °C < T < -38 °C. Additionally, the PSAC continuously observed the integrating sphere through the chopper. The DN was corrected using two G(T) results as T changed. The experimental data showed that the DN decreased by 1.08% when the T decreased from -38 °C to -61 °C, and these fluctuations were corrected to 0.38% and 0.34% with $G_{ins}(T)$ and $G_{det}(T)$, respectively. The DN values yielded before and after correction are shown in Figure 19. The first half of the $G_{det}(T)$ correction result displayed a small uptick, which may have been due to the fast cooling rate of the PST and the relatively higher measurement temperatures caused by the thermal resistance between the photosensitive surface and the thermal resistor of the detector. The smaller temperature change rate observed during the second half of the experiment resulted in a significant uptick reduction. In fact, the temperature change rate on the photosensitive surface of the detector was smaller on orbit than in this experiment, and temperature correction mitigated most variations. For this, when RSTC is applied to remote sensors operated in an environment with rapid temperature changes, the thermal resistance between the thermistor and the target should be reduced as much as possible to avoid deviations in the correction results caused by temperature hysteresis.

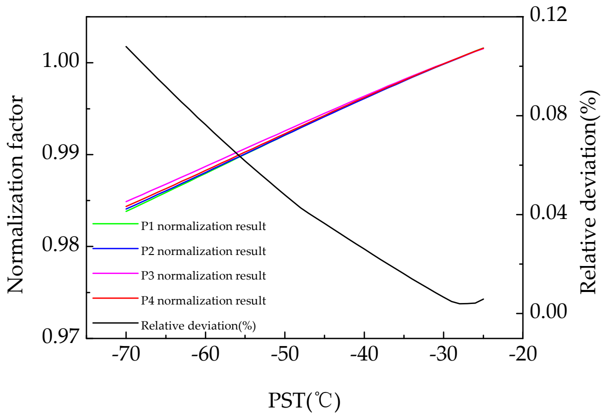

Figure 18. Comparison of the temperature characteristic consistency for 4 cells at 2250 nm. The experimental results indicated that their responsivity temperature dependences were generally consistent, and the maximum relative deviation was 0.11% in the temperature range of −70 °C < T < −25 °C.

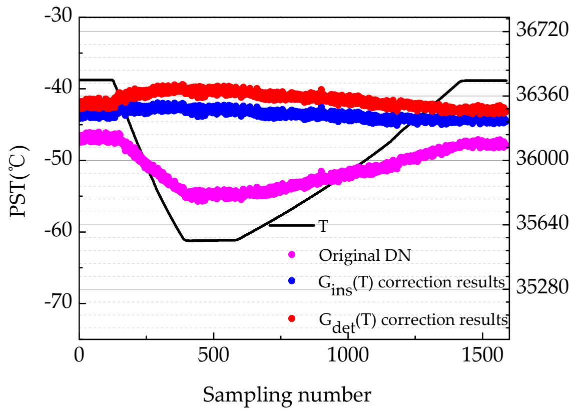

Figure 19. Comparison of two G(T) correction effects. The 1.08% fluctuation in DN when the T decreased from −38 °C to −61 °C was corrected to 0.38% and 0.34%, respectively, with $G_{det}(T)$ and $G_{ins}(T)$.

4.4. On-Orbit Application of RTDC

The DN from one scene observed by PSAC-B on 7 November 2020 included 130 scanning cycles of observations. The detector temperature controller and instrument thermal controller of the PSAC operated normally on orbit, and the PST was basically stable at approximately −61 °C, with a change of approximately 0.06°C. The radiation intensity information observed at the nadir and the $G_{ins}(T)$ correction-induced DN change in the 2250 nm channel are shown in Figure 20. After $G_{ins}(T)$ correction, the DN values of the 2250 nm channel increased by approximately 1.37%. As shown in Figure 20, the continuous-origin DN value after the 100th sampling point was constantly less than 1000 because the PSAC nadir was flying over Bohai Bay in China at that time.

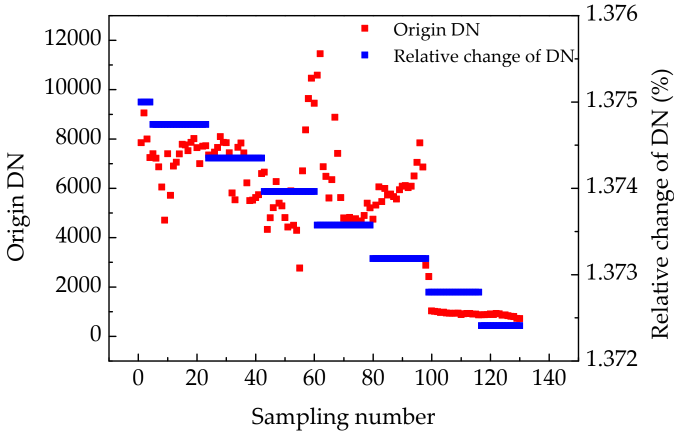

Figure 20. On-orbit application of G(T). The DN values at the nadir of the 2250 nm channel increased by approximately 1.37% with G(T) correction.

5. Conclusions

An experiment and a correction method for the responsivity temperature dependence in the SWIR channels of the PSAC are given in this article. An instrument-level thermal vacuum experiment and the detector-level experiment were carried out, respectively, and the curve of the relative responsivity change with the PST was obtained. Additionally, the consistency of the results obtained by the two experimental methods was assessed. The two types of experiments show that the detector responsivity of the 2250 nm band with about 35 °C PST difference between laboratory-based radiometric tests (PST≈-30 °C) and on-orbit operation (PST ≈ -65 °C) was reduced by approximately 1.3% and 1.5%, respectively. The temperature dependence in the SWIR channel was corrected to ensure the on-orbit applicability of the laboratory-based absolute radiometric calibration results and the atmospheric correction accuracy of the PSAC. The good consistency between the two experimental results indicates the effectiveness of the detector-level test for this type of detector.

Compared with the instrument-level test in harsh conditions, the detector-level test reveals the key impacts that the substitution test system may have on the test results and verifies the feasibility of using the substitution test when obtaining RTDC parameters. In addition, in practical applications, there is a need to consider possible influences in the detector-level test, such as the differences in characteristic parameters of the detector between the test and the detectors actually used in the instrument and the differences in the experimental system. Finally, as an exercise, the potential low-cost detector-level experimental approach explored in this paper provides an experimental reference for studies involving other remote sensors used for similar issues.

Author Contributions: Conceptualization, H.D., Z.L. and F.T.; Methodology, H.D. and F.T.; Software, X.L., F.T., M.L., L.Y. and Z.S.; Validation, H.D., P.Z. and M.S.; Formal analysis, H.D.; Investigation, H.D.; Resources, Z.L., Q.C., P.Z., M.S. and J.H.; Data curation, H.D., C.L. and X.Z.; Writing—original draft, H.D.; Writing—review & editing, H.D., Z.L. and F.T.; Visualization, H.D. and L.Y.; Supervision, Z.L.; Project administration, Z.L., and J.H.; Funding acquisition, Z.L., and J.H. All authors have read and agreed to the published version of the manuscript.

Funding: This research was funded by the National Natural Science Foundation of China (Grant No. 42275144), the HFIPS Director's Fund (Grant No. YZJJ202201-TS), and the K. C. Wong Education Foundation (Grant No. GJTD-2018-15).

Institutional Review Board Statement: Not applicable.

Informed Consent Statement: Not applicable.

Data Availability Statement: Data is contained within the article.

Conflicts of Interest: The authors declare no conflict of interest.

References

1. Lei, X.; Liu, Z.; Tao, F.; Hou, W.; Huang, H.; Xie, Y.; Zhao, X.; Dong, H.; Zou, P.; Song, M.; et al. Geolocation Error Estimation Method for the Wide Swath Polarized Scanning Atmospheric Corrector Onboard HJ-2 A/B Satellites. *IEEE Trans. Geosci. Remote Sens.* **2022**, *60*, 1–9. [CrossRef]
2. Lei, X.; Liu, Z.; Tao, F.; Zhao, X.; Hou, W.; Huang, H.; Xie, Y.; Dong, H.; Zou, P.; Song, M.; et al. Data preprocessing methods and procedures for the wide swath polarized scanning atmospheric corrector onboard HJ-2A/B satellites. *SPIE* **2022**, *12169*, 2029–2034. [CrossRef]
3. Li, Z.; Xie, Y.; Hou, W.; Liu, Z.; Bai, Z.; Hong, J.; Ma, Y.; Huang, H.; Lei, X.; Sun, X.; et al. In-Orbit Test of the Polarized Scanning Atmospheric Corrector (PSAC) Onboard Chinese Environmental Protection and Disaster Monitoring Satellite Constellation HJ-2 A/B. *IEEE Trans. Geosci. Remote Sens.* **2022**, *60*, 4108217. [CrossRef]
4. Xie, Y.; Hou, W.; Li, Z.; Zhu, S.; Liu, Z.; Hong, J.; Ma, Y.; Fan, C.; Guang, J.; Yang, B.; et al. Columnar Water Vapor Retrieval by Using Data from the Polarized Scanning Atmospheric Corrector (PSAC) Onboard HJ-2 A/B Satellites. *Remote. Sens.* **2022**, *14*, 1376. [CrossRef]
5. Shi, Z.; Hou, W.; Mei, L.; Sun, L.; Jia, C.; Ying, Z.; Li, K.; Xu, H.; Liu, Z.; Ge, B.; et al. Aerosol Optical Depth Retrieval Based on Neural Network Model Using Polarized Scanning Atmospheric Corrector (PSAC) Data. *IEEE Trans. Geosci. Remote Sens.* **2022**, *60*, 4109018. [CrossRef]
6. Li, Z.; Hou, W.; Hong, J.; Fan, C.; Wei, Y.; Liu, Z.; Lei, X.; Qiao, Y.; Hasekamp, O.P.; Fu, G.; et al. The polarization crossfire (PCF) sensor suite focusing on satellite remote sensing of fine particulate matter PM2.5 from space. *J. Quant. Spectrosc. Radiat. Transf.* **2022**, *286*, 108217. [CrossRef]
7. Dong, H.; Liu, Z.; Zou, P.; Hong, J. Background radiation response evaluation of InGaAs detectors. *SPIE* **2018**, *10832*, 424–433. [CrossRef]
8. Zhu, S.-s.; Zou, P.; Song, M.-x.; Zhao, K.-x.; Ling, M.-c.; Liu, Z.-h.; Qiu, Z.-w.; Hong, J. High-precision temperature control scheme and verification for space-borne infrared detectors. *SPIE* **2019**, *11023*, 52–58. [CrossRef]
9. Adamczyk, M.; Kamiński, M.; Sitnik, R.; Bogdan, A.; Karaszewski, M. Effect of temperature on calibration quality of structured-light three-dimensional scanners. *Appl. Opt.* **2014**, *53*, 5154–5162. [CrossRef]
10. Popoola, O.A.M.; Stewart, G.B.; Mead, M.I.; Jones, R.L. Development of a baseline-temperature correction methodology for electrochemical sensors and its implications for long-term stability. *Atmos. Environ.* **2016**, *147*, 330–343. [CrossRef]
11. Xiong, J.; Toller, G.; Chiang, V.; Sun, J.; Esposito, J.; Barnes, W. *MODIS Level 1B Algorithm Theoretical Basis Document*; NASA MODIS Characterization Support Team: Washington, DC, USA, 2005.
12. Barnes, R.A.; Holmes, A.W.; Barnes, W.L.; Esaias, W.E.; Mcclain, C.R. *SeaWiFS Technical Report Series. Volume 23: SeaWiFS Prelaunch Radiometric Calibration and Spectral Characterization*; NASA: Greenbelt, MD, USA, 1994.
13. Eplee, R.; Patt, F.; Meister, G.; Franz, B.; Bailey, S.; McClain, C. On-orbit calibration of SeaWiFS: Revised temperature and gain corrections. *SPIE* **2007**, *6677*, 146–160. [CrossRef]
14. Berjón, A.J.; Torres, B.; Toledano, C.; Podvin, T.; Blarel, L.; Prats, N.; Goloub, P.; Cachorro, V. Characterization of temperature sensitivity of sun photometers by field comparison with a reference instrument. *J. Aerosol Sci.* **2013**, *59*, 1–5. [CrossRef]
15. Andor, G. Temperature dependence of high accuracy photometer heads. *Appl. Opt.* **1989**, *28*, 4733_1–4734. [CrossRef] [PubMed]
16. Giles, D.M.; Sinyuk, A.; Sorokin, M.G.; Schafer, J.S.; Smirnov, A.; Slutsker, I.; Eck, T.F.; Holben, B.N.; Lewis, J.R.; Campbell, J.R.; et al. Advancements in the Aerosol Robotic Network (AERONET) Version 3 database—Automated near-real-time quality control algorithm with improved cloud screening for Sun photometer aerosol optical depth (AOD) measurements. *Atmos. Meas. Tech.* **2019**, *12*, 169–209. [CrossRef]
17. Holben, B.N. AERONET Annual Review. 2008. Available online: http://aeronet.gsfc.nasa.gov/new_web/-AERONET_Annual_Review08_final.pdf (accessed on 1 July 2022).
18. Chen, S.; Li, Y.; Cao, F.; Zhang, Y. Calibration of Automatic Sun Photometer with Temperature Correction in Field Environment. *Remote Sens.* **2022**, *14*, 66. [CrossRef]
19. Yao, P.; Tu, B.; Xu, S.; Yu, X.; Xu, Z.; Luo, D.; Hong, J. Non-uniformity calibration method of space-borne area CCD for directional polarimetric camera. *Opt. Express* **2021**, *29*, 3309–3326. [CrossRef]
20. Mishchenko, M.I.; Cairns, B.; Kopp, G.; Schueler, C.F.; Fafaul, B.A.; Hansen, J.E.; Hooker, R.J.; Itchkawich, T.; Maring, H.B.; Travis, L.D. Accurate Monitoring of Terrestrial Aerosols and Total Solar Irradiance: Introducing the Glory Mission. *Bull. Am. Meteorol. Soc.* **2007**, *88*, 677–692. [CrossRef]
21. Hansen, J.E.; Travis, L.D. Light scattering in planetary atmospheres. *Space Sci. Rev.* **1974**, *16*, 527–610. [CrossRef]
22. Xiong, X.; Aldoretta, E.; Angal, A.; Chang, T.; Wu, A. Terra MODIS: 20 years of on-orbit calibration and performance. *J. Appl. Remote Sens.* **2020**, *14*, 037501. [CrossRef]
23. Liu, Z.; Luo, D.; Zou, P.; Chen, D.; Lu, M.; Hong, J. A Kind of Signal Drift Dynamic Correcting Method and Device. China. CN108363445B, 28 July 2020.
24. Li, B.; Zhang, S.Y.; Jiang, J.C.; Liu, D.Q.; Zhang, F.S. Recent progress in improving low-temperature stability of infrared thin-film interference filters. *Opt. Express* **2005**, *13*, 6376–6380. [CrossRef]

25. Stolberg-Rohr, T.; Hawkins, G.J. Spectral design of temperature-invariant narrow bandpass filters for the mid-infrared. *Opt. Express* **2015**, *23*, 580–596. [CrossRef] [PubMed]
26. González-Cuevas, J.; Refaat, T.; Abedin, M.N.; Elsayed-Ali, H. Modeling of the temperature-dependent spectral response of $In_{1-\chi}Ga_{\chi}Sb$ infrared photodetectors. *Opt. Eng.* **2006**, *45*, 044001.